Enhanced Lithium Stroage Capability of $FeF_3 \cdot 0.33H_2O$ Single Crystal with Active Insertion Site Exposed

Guanghai Chen[a], Xingzhen Zhou[a,b], Ying Bai[a,*], Yifei Yuan[c], Mizi Chen[a], Lu Ma[c], Guoqiang Tan[c], Yu Li[a], Junping Hu[d], Zhaohua Wang[a], Feng Wu[a,e], Jun Lu[c*], Chuan Wu[a,e*]

[a] Beijing Key Laboratory of Environmental Science and Engineering, School of Materials Science and Engineering, Beijing Institute of Technology, 5# South Zhongguancun Street, Beijing 100081, China

[b] National Active Distribution Network Technology Research Center, Beijing Jiaotong University, 3# Shangyuancun Street, Beijing 100044, China

[c] Chemical Sciences and Engineering Division, Argonne National Laboratory, 9700 South, Cass Avenue, Lemont, IL 60439, USA

[d] School of Science, Nanchang Institute of Technology, Nanchang 330099, China

[e] Collaborative Innovation Center of Electric Vehicles in Beijing, Beijing 100081, China

∗ Corresponding author.
E-mail address: membrane@bit.edu.cn (Y. Bai), junlu@anl.gov (J. Lu), chuanwu@bit.edu.cn (C. Wu)

Abstract

Iron fluoride cathode for lithium batteries intrigues researchers for decades due to high capacity and low cost, but suffers from poor electronic and ionic conductivity. Hierarchical micro/nano construction with preferred growth orientation can shorten ion diffusion pathway and facilitate electron transportation without inducing side reactions. Here, the octagonal single crystal slices constituting the $FeF_3 \cdot 0.33H_2O$ hierarchical microsphere provides more lithium ions intercalation positions (4c sites), which is confirmed by SAED and XRD characterizations. Benefiting from the artful structure, experimental studies demonstrate that the well designed $FeF_3 \cdot 0.33H_2O$ single crystal (FFH-S) delivers 30 mAh g^{-1} higher capacity (172 mAh g^{-1} at 0.1C) than the common $FeF_3 \cdot 0.33H_2O$ polycrystal (FFH-P). In-situ XRD combined with theoretic calculation elucidate the difference in lithium storage capacity. Instructive

argument that single crystal octagon slices with [001] growth orientation provide more active sites for lithium ions intercalation contributes to the preparation of high performance iron fluoride cathode materials for rechargeable battery.

Keywords: $FeF_3 \cdot 0.33H_2O$; single crystal; hierarchical micro/nano structure; preferred growth orientation; in situ XRD; first-principles calculation

1. Introduction

Since first commercialized by Sony in 1991, lithium ion batteries (LIBs) based on $LiCoO_2$ cathode and graphite anode have reformed the portable mobile electronic devices, including laptop computers, microchips, cell phones and digital cameras.[1-5] However, ever-increasing energy density demand calls for next-generation lithium batteries, especially advanced electrode materials. Recently, the revival of lithium metal anode makes it possible to use lithium-free cathode materials for next-generation energy-dense lithium batteries. Once the anode is replaced by lithium metal, the working voltage and energy density of full cell can be boosted, because lithium has the highest theoretical capacity (3860 mAh g^{-1}) and the lowest reduction potential (-3.04V vs. standard hydrogen electrode).[6-7]

Over the last two decades, iron trifluoride has aroused incessant interest due to a high theoretical capacity of 237 mAh g^{-1} ($1e^-$ transfer) at an average potential ~2.7 V, a larger theoretical capacity of 712 mAh g^{-1} ($3e^-$ transfer), low toxicity, low cost and good thermal stability.[8-13] However its practical application is restrained by low electronic conductivity due to the strong ionic bond between Fe and F, and the sluggish kinetics.[14-15] Considerable efforts have been devoted to improve the electronic conductivity via mixing conductive materials and doping cationic, but the cycling stability is unsatisfactory.[9, 13, 16-20] It is reported that trace hydration water in the center of open framework iron fluoride compounds with one-dimension (1D) tunnel is helpful to improve the electronic conductivity and boost Li^+ diffusion, especially stabilize the structure.[21-26] $FeF_3 \cdot 0.33H_2O$ is especially eye-catching among

them due to its special tunnel structure.[21-22, 25-30] In $FeF_3 \cdot 0.33H_2O$ lattice, two kinds of FeF_6 octahedrons are connected via corner-sharing to generate special hexagonal cavities with water molecules in the center. All the O-F distances in the huge hexagonal cavities are more than 3 Å, resulting in the rapid Li^+ transportation.[21-22] Even though, electronic conductivity and kinetics of $FeF_3 \cdot 0.33H_2O$ are also unable to meet the application requirements. Likewise, on one hand, adding conductive additive, especially carbon nanotube and graphene is the common route to improve electronic conductivity.[24, 27, 31-32] On the other hand, preparing nano-structure is generally used to shorten Li^+ migration pathway.[22, 24-25, 33] For example, Li et al.[25] prepared nanostructured $FeF_3 \cdot 0.33H_2O$ in the ambience of [Bmim][BF_4] ionic liquid, reversible capacity of 154 mAh g^{-1} was reached at a current density of 14 mA g^{-1} during the voltage range of 1.6 – 4.5 V. Tan et al.[33] synthesized compound with a mixed crystal structure of $FeF_3 \cdot 3H_2O$ and $FeF_3 \cdot 0.33H_2O$, delivering an initial discharge capacity of 106.7 mAh g^{-1} at 0.5C. After ball-milled with 15wt % acetylene black and heat-treatment, the size of particle was greatly reduced and $FeF_3 \cdot 0.33H_2O$/C nanocomposite achieved a discharge capacity of 160.2 mAh g^{-1}. However, side reaction easily occurs between nano-structured $FeF_3 \cdot 0.33H_2O$ and electrolyte, which results in bad stability.

Three dimensional (3D) hierarchical micro/nano structure with active nanoplate exposed is conducive to not only shortening Li^+ migration pathway but also avoiding the side reactions.[34-36] Designing such an artful structure is generally difficult. As the active plates have higher surface energy, which have the tendency to disappear and

the surface of the crystal will be dominated by low-energy plates during the process of crystal growth.[37] Herein, we report a controllable approach to synthesize 3D hierarchical $FeF_3 \cdot 0.33H_2O$ consist of single crystal octagon slices with preferred [001] growth orientation. High resolution transmission electron microscopy (HRTEM) and the selected area electron diffraction (SAED) characterizations uncover that the single crystal slices provides more intercalation positions (4c sites) for lithium ions. In situ X-ray diffractions (XRD) analysis demonstrate lithium ions insert/de-insert mainly into (002) and (220) interlaminations. First-principles calculation manifests that this unique single crystal structure with preferred [001] orientation has a 0.32 eV lower lithium adsorption energy than that with preferred [110] orientation, well agreement with the result of experiment.

2. Result and discussion

The synthesis of $FeF_3 \cdot 0.33H_2O$ hierarchical micro/nano sphere is schematically depicted in **Figure 1**a. A detail description is given in the experimental section. Briefly, $FeF_3 \cdot 0.33H_2O$ hierarchical micro/nano spheres were prepared by liquid precipitation and following a heat treament to remove part of crystal water. During the precipitation, the octagon slices constituted self-assemblly $FeF_3 \cdot 3H_2O$ hierarchical micro/nano spheres in the presence of the polyethylene glycol (PEG, MW=20000) dispersant. XRD pattern of the as-prepared $FeF_3 \cdot 3H_2O$ precursor is shown in Figure S1 in the Supporting Information. The filed-emission scanning electron microscope (SEM) images and transmission electron microscopy (TEM) image (**Figure 1**b-d)

show that $FeF_3 \cdot 0.33H_2O$ powders have a hierarchical nanoplate/microsphere morphology with diameters of ~16 μm, which are composed of knife edge-like slices. The composition of $FeF_3 \cdot 0.33H_2O$ is examined by energy dispersive X-ray (EDX) in **Figure 1**e-g. The element distribution mapping indicates Fe, F and O are uniformly distributed and without any phase separation. The selected area electron diffraction (SAED) characterizations and high-resolution transmission electron microscope (HRTEM) were carried out to uncover the crystal structure of the octagon slice (**Figure 1**d). From the HRTEM image in **Figure 1**h, lattice spacing of (002) plane can be indexed as 0.37nm. And as shown in **Figure 1**i, the nanoplate is viewed along [1-10] zone axis with (002), (112) and (110) lattice diffractions with spaces of 0.37nm, 0.32nm and 0.64nm. Not just the SAED pattern of one corner edge in **Figure 1**d, but other SAED patterns (Figure 2**s**) of other corner edges demonstrate that the frontal facet is dominated by (220) plane of $FeF_3 \cdot 0.33H_2O$.

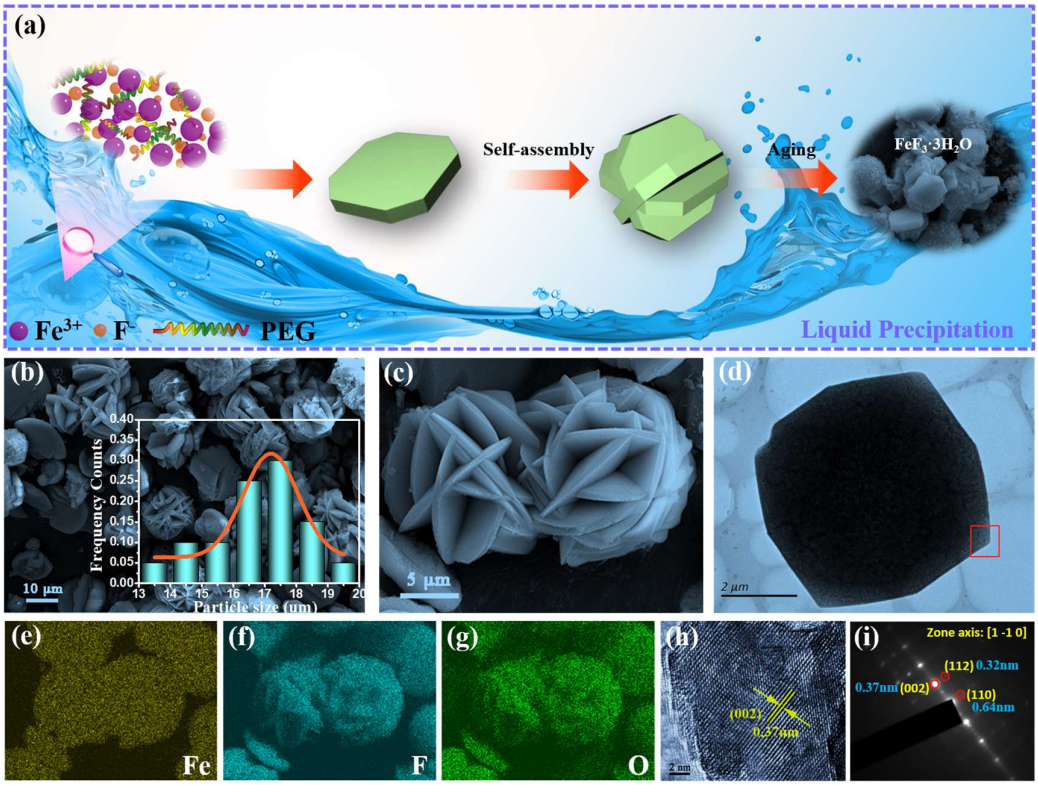

Figure 1. a) Schematic diagram of preparing $FeF_3 \cdot 0.33H_2O$, b) and c) SEM images of $FeF_3 \cdot 0.33H_2O$ hierarchical micro/nano spheres (inset in b is the grain size distribution map), d) TEM image of octagon slice constituting $FeF_3 \cdot 0.33H_2O$ hierarchical sphere, e-f) EDX maping of $FeF_3 \cdot 0.33H_2O$ hierarchical micro/nano spheres based on c, h) high resolution TEM of $FeF_3 \cdot 0.33H_2O$ and i) SAED pattern of one corner region in d.

It is difficult to evaluate the crystal indices of the side of the octagon slice by SAED because of the large vertical thickness. Fortunately, the powder X-ray diffraction (XRD) as well as Rietveld refinement pattern of $FeF_3 \cdot 0.33H_2O$ provides some information about the side of the octagon slice. As shown in **Figure 2**a, all diffraction peaks can be well indexed to an orthorhombic structure (space group: Cmcm), but the ratio of the two diffraction peak intensity ($R=I_{002}/I_{220}$, 1.02) is greater than that of the standard ratio (0.86) of randomly oriented powders (JCPDS card No.76-1262). And a large mismatch of (002) line based on the Rietveld refinements with reliable R_{wp} and R_p fitting factors can be observed. Same results can be got no

matter how the powder sample is loaded on the object stage of XRD. According to the Bragg's law, the enhanced relative intensity of (002) diffraction peak manifests that (002) planes are perpendicular to the X-ray beam. On account of the hierarchical micro/nano sphere, most of octagon slices do not lie flat and the X-ray beam can be vertical to (002) planes. Therefore, the relative intensity of (002) diffraction peak is enhanced. Namely, the lateral of the octagon slice is dominated by (002) plane of $FeF_3 \cdot 0.33H_2O$, as illustrated in **Figure 2**b.

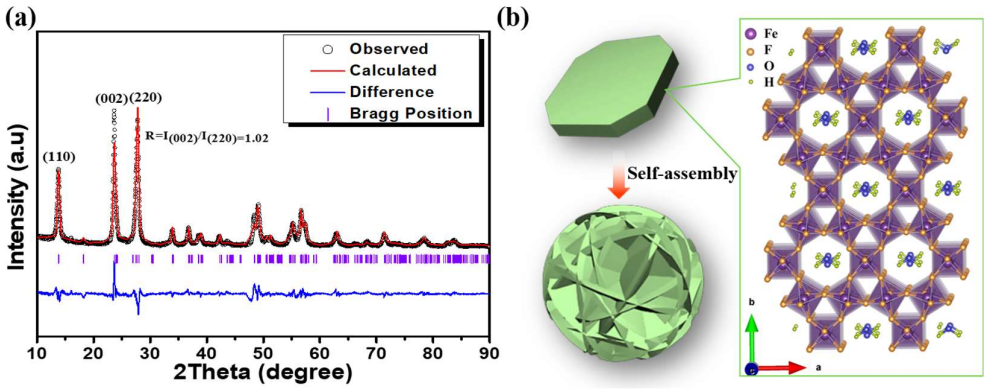

Figure 2. a) XRD pattern and b) schematic diagram of diffraction and cryctal structure of the lateral of the octagon slice.

Electrochemical performances of this hierarchical micro/nano $FeF_3 \cdot 0.33H_2O$ sphere consist of single crystal octagon slice with [001] growth orientation (named as FFH-S) are investigated. For comparison, $FeF_3 \cdot 0.33H_2O$ possessing same morphology with polycrystal octagon slices (named as FFH-P) was synthesized and characterized. Detailed structure and morphology characterizations of FFH-P are shown in Figure S3 in the Supporting information. The galvanostatic discharge-charge voltage profiles of two samples at 1st, 2nd, and 3rd cycles are shown in **Figure 3**a-b. Within the cut off voltage of 2.0 - 4.5 V, FFH-S and FFH-P show the same initial discharge plateaus at

approximately 2.7 V and 2.6 V respectively, corresponding to Li^+ intercalation into the $FeF_3 \cdot 0.33H_2O$ forming $Li_xFeF_3 \cdot 0.33H_2O$ in the first cycle. And the initial charge plateaus at approximately 3.2 V and 3.0 V respectively can be also observed, which are corresponding to Li^+ deintercalation from $Li_xFeF_3 \cdot 0.33H_2O$.

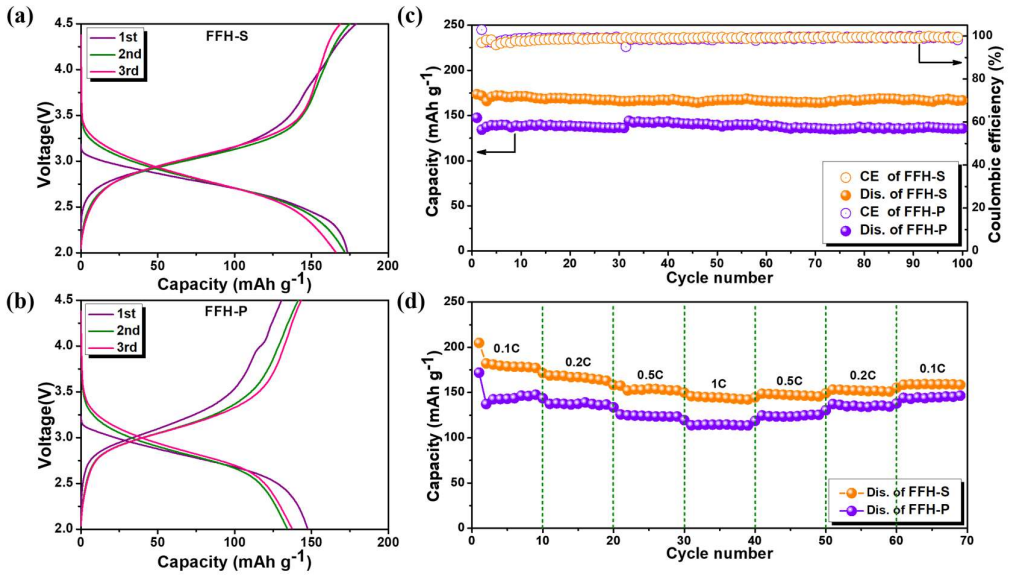

Figure 3. The galvanostatic discharge-charge voltage profiles of two samples at 1st, 2nd, and 3rd cycles a) FFH-S and b) FFH-P, c) cycling performance and d) rate performances of FFH-S and FFH-P at various current densties (1C=200 mA g^{-1}).

However, as presented in **Figure 3**c, FFH-S delivers an initial discharge capacity of 173.5 mAh g^{-1} and reversible capacity of 167 mAh g^{-1} at 0.1C (1C = 200 mAh g^{-1}) with a slight capacity decay due to formation of solid electrolyte interphase (SEI) forming[38-40]. For FFH-P, although an initial capacity of 147.5 mAh g^{-1} is achieved, only 134.3 mAh g^{-1} is preserved in second cycle. After 100 cycles, a discharge capacity of 166.9 mAh g^{-1} is still preserved. And it is always 20 - 30 mAh g^{-1} lower than that of FFH-P over the 100 cycles. Such a capacity gap between FFH-S and FFH-P exists not only at a current density of 0.1C but also at higher current densities.

As shown in **Figure 3**d, the discharge capacities of FFH-S are always higher than that of FeF-P at 0.1C, 0.2C, 0.5C and even 1C. As a result, lithium storage capability of $FeF_3 \cdot 0.33H_2O$ material with single crystal octagon slices is much better than the other one.

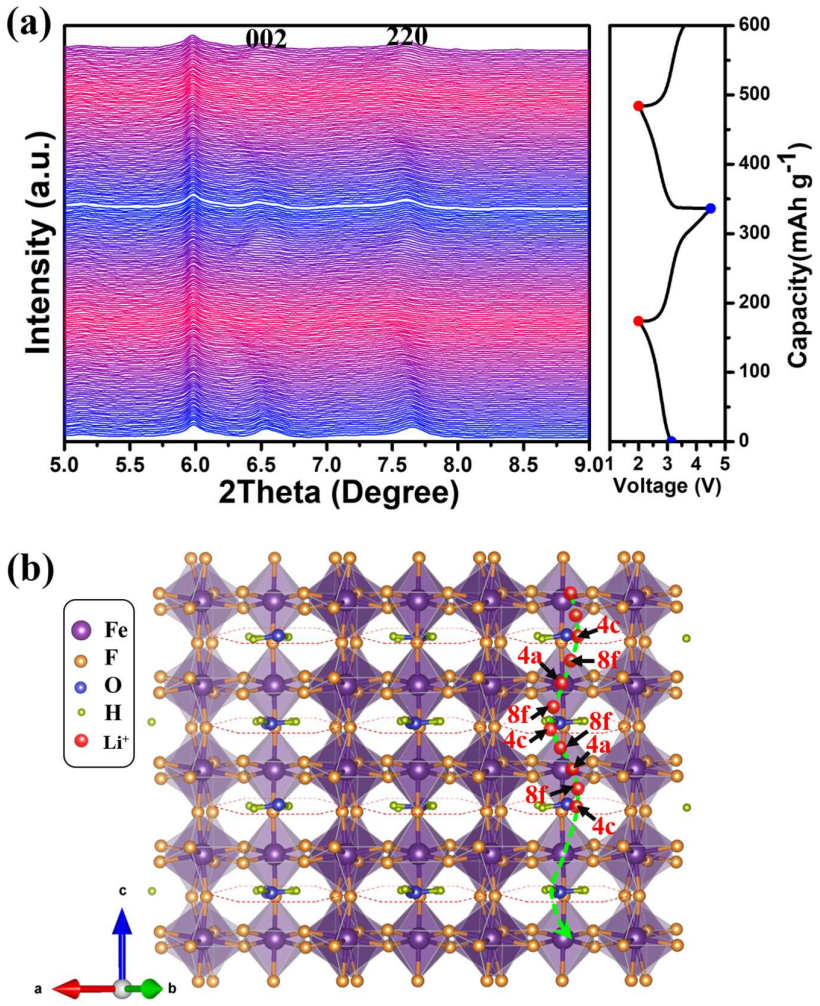

Figure 4. a) In situ SAXRD characterization in the 2θ range from 5° to 9° of FFH-S during the first two discharge-charge cycles and b) crystal structure of $FeF_3 \cdot 0.33H_2O$ viewing in [110] direction (dotted boxes in red is the hexagon tunnel for Li^+ migration, dottted line in green is the migration path).

To further investigate the capacity difference, it is necessary to monitor the crystal structure variation by in-situ small angle XRD characterization (SAXRD). The

SAXRD in the 2θ range from 5° to 9° of FFH-S during the discharge-charge cycles is shown in **Figure 4**a (SAXRD in wider range is presented in Figure S4). (002) and (220) peaks shift to lower angle during discharge and the peak intensity reduce, corresponding to intercalation of Li^+, delivering a discharge capacity of 173 mAh g^{-1}. Then, they shift to higher angle and become sharper during charge, corresponding to deintercalation of Li^+ and delivering a charge capacity of 163 mAh g^{-1} well agreement with the discharge-charge curve in the right. Undoubtedly, the shift of diffraction peak is related to the intercalation site and migration path of Li^+. As dissected in **Figure 4**b, it is reported that lithium ions are only possible insert at Wyckoff positions as 4a, 4c, 8e, 8f and 8g. Thereinto, 4c sites on the side of oxygen atoms are the most stable intercalation site for Li^+ due to the lowest formation energy. And Li^+ migrates along positions as 4c, 8f, 4a, 8f, 4c, 8f, 4a, 8f, et. al.[30] Explicitly, the intercalation of Li^+ in 4c sites increase the interlayer spacing of (002) plane. And the intercalation of Li^+ in 4a sites, the middle point of every two adjacent oxygen atoms, increase the interlayer spacing of (220) plane. According to above structure analyses based on SAED and XRD, in the single crystal octagon slices of FFH-S, 4c and 4a sites are fully orderly exposed in the electrolyte. Therefore more lithium ions insert the hexagon tunnel, resulting in higher capacity than FFH-P.

In order to understand the improved lithium storage capability of $FeF_3 \cdot 0.33H_2O$ consist of single crystal octagon slice with [001] growth orientation, the first-principles studies are carried out to calculate the adsorption energy (E_{ad}) of Li atom in the $FeF_3 \cdot 0.33H_2O$ with [001] and [110] preferred growth orientation

respectively, because lithium ion mainly insert into (002) and (220) crystal layers according to above in-situ XRD results. As shown in **Figure 5**a, unit cell of $FeF_3 \cdot 0.33H_2O$ with 60 atoms (F:Fe:H:O = 36:12:8:4) is optimized. $FeF_3 \cdot 0.33H_2O$ consists of huge hexagonal cavity tunnels which are formed by the connecting of six corner-sharing FeF_3 perovskites, and water molecules which alternately ranged in opposite directions in the center of hexagonal cavities.[30] The (220) plane is formed via tortile octahedral FeF_6 corner-sharing (the blue section); (002) plane is precisely the cross section of the hexagon cavity tunnel structure. The 1 × 2 × 1 supercell of $FeF_3 \cdot 0.33H_2O$ is built to form the atomic model of FFH-S with [001] growth orientation. Only the period property in the c-direction is kept, the other two directions are cut and then added by more the 15 Å vacuum layers (**Figure 5**b). Similarly, the 1 × 1 × 2 supercell of $FeF_3 \cdot 0.33H_2O$ is built to form the atomic model with [110] growth orientation. Only the period property in the a- and b-directions are kept, and the c-direction is cut and then added by more the 15 Å vacuum layers (**Figure 5**c).

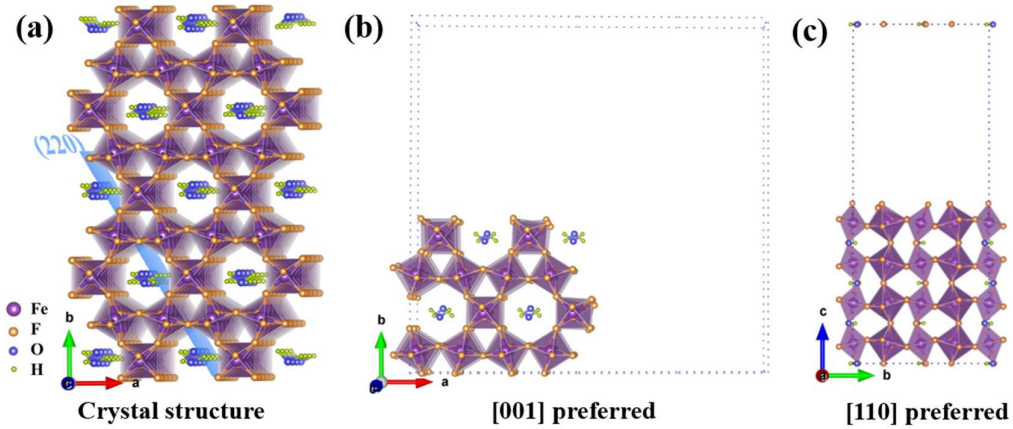

Figure 5. a) Crystal structure of $FeF_3 \cdot 0.33H_2O$ (plane in blue is the (220) lattice plane), b) 1 × 2 × 1 supercell of FeF3·0.33H2O built to form the atomic model with

[001] growth orientation, and c) 1 × 1 × 2 supercell built to form the atomic model with [110] growth orientation.

Through test, the most stable structure of lithium atom intercalation is 4c site, which is in agreement with previous work.[30] The adsorption energy (E_{ad}) of Li atom in the $FeF_3{\cdot}0.33H_2O$ or its preferred models is defined as:

$$E_{ad} = E_{\mathrm{Li}_x\mathrm{FeF_3{\cdot}0.33H_2O}} - E_{\mathrm{FeF_3{\cdot}0.33H_2O}} - E_{Li} \qquad (1)$$

where E_{Li} is the cohesive energy in metal Li, $E_{\mathrm{Li}_x\mathrm{FeF_3{\cdot}0.33H_2O}}$ and $E_{\mathrm{FeF_3{\cdot}0.33H_2O}}$ are the total energies of $FeF_3{\cdot}0.33H_2O$ or it preferred models with and without Li adsorption, and specific values corresponding to sample FFH-S and FFH-P are listed in **Table 1**. The calculation result shows that the Li^+ adsorption energy of the $FeF_3{\cdot}0.33H_2O$ with preferred [001] orientation is 0.32 eV lower than that of the $FeF_3{\cdot}0.33H_2O$ with preferred [110] orientation, which means that lithium ions prefer to intercalate into the $FeF_3{\cdot}0.33H_2O$ with active 4c sites exposed.

Table 1. Energies of $FeF_3{\cdot}0.33H_2O$ with [001] and [110] preferred model before and after absorbing lithium atom.

Preferred Model	$E_{\mathrm{Li}_x\mathrm{FeF_3{\cdot}0.33H_2O}}$/eV	$E_{\mathrm{FeF_3{\cdot}0.33H_2O}}$/eV	E_{Li}/eV	E_{ad}/eV
[001]	-653.17	-645.06	-1.89	-6.22
[110]	-637.78	-629.99	-1.89	-5.90

Extremely similar lithium ion diffusion characteristics of two samples are obtained according to a reliable and accurate galvanostatic intermittent titration technique (GITT), which is employed on the second cycle (Figure S5). An interval of 10 min discharging/charging at a small current density of 20 mA g^{-1} and a long time interval of 60 min are performed to achieve steady-state (E_s). And this process is carried out

repeatedly in the voltage of 2.0 - 4.5V. Figure S5a presents the discharge GITT curves of two samples as a function of time in the potential range of 2.0 - 4.5 V. The longer test time of FFH-S than that of FFH-P indicates that the discharge capacity of the former is higher than that of the latter, which is also consistent with the galvanostatic charge-discharge results. The chemical diffusion coefficient of Li^+ is calculated according to Eq. (2) derived by Weppner and Huggins [41-43]

$$D_{Li^+} = \frac{4}{\pi}\left(\frac{mV_M}{MS}\right)^2 \left(\frac{dE/dx}{dE/d\tau^{1/2}}\right)^2 \quad (t \ll L^2/D_{Li}) \qquad (2)$$

where M and m are the molecular weight and mass of $FeF_3 \cdot 0.33H_2O$, respectively. V_M ($cm^3\ mol^{-1}$) is the molar volume of the active materials, which is $4.28 \times 10^{-4} m^3\ mol^{-1}$ for $FeF_3 \cdot 0.33H_2O$ deduced from the crystallographic data, S (cm^2) is the total contact area between the electrolyte and electrodes, and L (cm) is the diffusion length. A single step titration at 2.90 V during the process is illustrated in Figure S5b with schematic labeling of different parameters. If the voltage (E) has a good linearity with the square root of interruption time ($\tau^{1/2}$) over the entire period of current flux, as shown in Figure S5c, Eq. (2) can be further simplified as Eq. (3) [44]

$$D_{Li^+} = \frac{4}{\pi\tau}\left(\frac{mV_M}{MS}\right)^2\left(\frac{\Delta E_s}{\Delta E_\tau}\right)^2 \qquad (3)$$

Based on Eq. (3) and GITT measurements, the diffusion coefficients of Li^+ at varied voltages can be obtained, as shown in Figure S5d. At the discharge platform (from 3.5 V to 2.8 V), the lithium ion diffusion coefficients (D_{Li+}) of both two samples decrease rapidly as a result of the decrease of concentration difference between inside and outside bulk phase. The smallest D_{Li^+} of FFH-S and FFH-P are $7.855 \times 10^{-14}\ cm^2\ s^{-1}$ and $9.575 \times 10^{-14}\ cm^2\ s^{-1}$, obtained at 2.83 V and 2.72 V respectively. At the discharge

process from 2.8 V to 2.3 V, the D_{Li+} of both FeF-M and FeF-P eventually approach to a constant value (~ 1.73×10^{-13} cm^2 s^{-1}). The similar D_{Li+} variation tendency of two samples demonstrates the same diffusion characteristics of Li^+. In summary, the difference of crystal structure of $FeF_3 \cdot 0.33H_2O$, which is induced by [001] crystal orientation, has a great influence on lithium storage capability but little impact on lithium diffusion characteristic. According to previous report,[30] Li^+ transport around the oxygen atoms with a S-shaped path inside the hexagonal tunnel. No matter through which crystal plane the lithium ions insert into the crystal, they transport inside the same tunnel. Therefore, the crystal orientation does not make difference in Li^+ diffusion characteristics.

3. Conclusions

In conclusion, $FeF_3 \cdot 0.33H_2O$ consist of octagon slices is formed via self assembly in ethanol solvent containing a surfactant, followed by a heat treatment process of $FeF_3 \cdot 3H_2O$ precursor. Crystal structure analyses based on SAED and XRD reveal that the octagon slice has a preferred [001] growth orientation and exposes (220) plane on top view. Benefitting from this artful structure, FFH-S exhibits enhanced lithium storage capcbility. In situ XRD demonstrates that lithium ions insert into and transport within the hexagonal tunnel. In this way, the single crystal slice provides more 4c sites for lithium ions intercalation, which has the lowest formation energy for lithium ions intercalation confirmed by the first-principles calculation, well agreement with experimental results. The reported findings contribute to the preparation of high

performance iron fluoride cathode materials for rechargeable battery.

4. Experimental Section

Synthesis of $FeF_3 \cdot 0.33H_2O$ materials: All chemical reagents were of analytical grade and used without further purification. Mixed solvent of ethanol (150 ml), deionized water (20 ml) and 15g polyethylene glycol (PEG 20000) dispersant was prepared in duplicate. One of them was mixed with iron (III) nitrate nonahydrate ($Fe(NO_3)_3 \cdot 9H_2O$) ethanol solution (160 ml, 0.25 $mol \cdot L^{-1}$) and the other was used to dissolve ammonium bifluoride NH_4HF_2 in a Teflon beaker. The molar ratio of $Fe^{3+}/F^-$is 1:3. The completely dissolved $Fe(NO_3)_3$ solution was pumped dropwise into the NH_4HF_2 solution, accompanied by magnetic stirring to obtain pale yellow precipitates after aging for 10 h at room temperature. After washed by deionzed water and ethanol alternately for three times, subsequently vacuum-dried at 80 ^oC for 12 h and cooled down naturally, the precipitates were obtained. To obtain iron fluoride with trace of hydration, the as-prepared precipitates were directly calcined at 300 ^oC for 3 h (The product is named FFH-P). Meanwhile, the as-prepared precipitates were pre-sintered at 200 ^oC for 3h to remove the hydration water and then 300 ^oC for 3h in argon atmosphere (The product is named FFH-S).

Material Characterization: Crystal structure was characterized by a Rigaku 2400 X-ray diffraction (XRD) with Cu Kα radiation (λ=0.15418nm) between 10° and 90° 2θ at a scan rate of 1^o 2θ min^{-1}. A filed-emission scanning electron microscope (FE-SEM) Quanta 250 and a high-resolution transmission electron microscope

(HR-TEM) HITACHI H-800 were employed to characterize the morphologies of as-prepared samples.

In situ small angle X-ray diffractions were carried out at the experimental station 13-BM-C of the Advanced Photon Source, Argonne National Laboratory. The X-ray beam was monochromated with silicon 311 crystal to 28.6 keV (0.434 Å), with 1 eV bandwidth. A Kirkpatrick-Baez mirror system was used to obtain a vertical × horizontal focus spot size of 20 μm × 30 μm, measured as full width at half maximum (FWHM). The diffraction pattern was collected in a transmission way, and the MAR165 Charge Coupled Device (CCD) detector (Rayonix) was placed about 180 mm away from the sample. The typical exposure time was 60 seconds for each diffraction pattern. The diffraction patterns were integrated and analyzed by the DIOPTAS software (Prescher and Prakapenka, 2015).

Electrochemical Measurements: The electrochemical performance was evaluated in coin-type cells (CR2025) assembled in an Ar-filled glove box (MBraun Labmaster 130). The working electrode was prepared by coating the slurry, which was composed of as-prepared cathode material, conductive additive Super P and polyvinylidene fluoride (PVDF) binder in N-methyl-2-pyrrolidinone (NMP) with a weight ratio of 8:1:1, on aluminum foil. Then, aluminum foil was dried in a vacuum oven at 80 ºC for 24 h. Lithium metal foil was used as the counter electrode and reference electrode, and Celgard 2400 was used as the separator. The electrolyte was 1M solution of $LiPF_6$ dissolved in a mixed solvent of ethylene carbonate (EC), dimethyl carbonate (DMC) and ethylene methyl carbonate (EMC) (1:1:1 by volume).

The galvanostatic charge–discharge tests and galvanostatic intermittent titration technique (GITT) were conducted on the battery measurement system (LAND CT2001A) at various rates with the cut-off potential range of 2.0 - 4.5 V *vs.* Li^+/Li.

First-principles calculation: Our calculation is based on density functional theory (DFT) using the plane-wave pseudopotentials[45] with exchange-correlation of Perdew-Burke-Ernzerhof (PBE)[46-47] form as implemented in the Vienna Ab initio Simulation Package (VASP).[48] A cutoff energy of 500 eV is employed for the plane wave expansion of the wave functions. Considering the strong correlation effects in iron element, electronic structure calculations and structural relaxations are performed by using a spin-dependent GGA plus Hubbard U (GGA+U) method.[49-50] Herein, the U value of Fe atom is set to be 4 eV.[30, 51] The Brillouin zone is sampled with 2 × 1 × 1 Monkhorst-Pack *k*-point mesh[52] for the structural optimization, and with 4 × 2 × 2 mesh for the electronic structure calculations. The convergence criteria for the total energy was set to 10^{-4} eV.

The surface energy of $FeF_3 \cdot 0.33H_2O$ with 60 atoms (F: Fe: H: O = 144:48:32:16) is calculated to quantify the stability of (220) and (002) plane by the first principles calculation. The 1 × 1 × 4 and 2 × 2 × 1 supercells of $FeF_3 \cdot 0.33H_2O$ are built to calculate the surface energies of (002) plane and (220) plane, respectively. The calaulation result shows that the surface of (002) plane (-1234.05eV) is 1.35eV higher than that of (220) plane (-1235.4eV). Therefore, the (002) plane has a tendency to disappear during the growth process and the surface should be gradually dominated by the (220) plane according to previous study.[37] Therefore, $FeF_3 \cdot 0.33H_2O$ with (220)

plane exposed is the thermodynamic equilibrium products for a long sintering time.

Supportting Information

Supportting Informantion is available from xxxxxxx.

Ackonwledgement

The present work is supported by the National Key R&D Program of China: Trackling Key Thchnology for Development and Industrialization of Power Lithium Ion Battery with High Specific Energy (Grant No. 2016YFB0100500).

Conflict of Interest

The authors declare no conflict of interest.

Reference

1. J.-M. Tarascon, M. A., Issues and challenges facing rechargeable lithium batteries.pdf *Nature* **2001**.
2. Peter G. Bruce, B. S., and Jean-Marie Tarascon, Nanomaterials for Rechargeable Lithium Batteries.pdf. *Angew. Chem. Int. Ed.* **2008,** *47*, 2930 – 2946.
3. Gibot, P.; Casas-Cabanas, M.; Laffont, L.; Levasseur, S.; Carlach, P.; Hamelet, S.; Tarascon, J. M.; Masquelier, C., Room-temperature single-phase Li insertion/extraction in nanoscale Li(x)FePO4. *Nature materials* **2008,** *7* (9), 741-7.
4. M. Armand, J.-M. T., Building better batteries. *Nature* **2008,** *451*, 652-657.
5. Kang, B.; Ceder, G., Battery materials for ultrafast charging and discharging. *Nature* **2009,** *458* (7235), 190-3.
6. Lin, D.; Liu, Y.; Cui, Y., Reviving the lithium metal anode for high-energy batteries. *Nat Nanotechnol* **2017,** *12* (3), 194-206.
7. Wu, F.; Yuan, Y.-X.; Cheng, X.-B.; Bai, Y.; Li, Y.; Wu, C.; Zhang, Q., Perspectives for restraining harsh lithium dendrite growth: Towards robust lithium metal anodes. *Energy Storage Materials* **2018,** *15*, 148-170.
8. Hong Li, P. B., Joachim Maier, Li-Storage via Heterogeneous Reaction in Selected Binary Metal Fluorides and Oxides. *Journal of The Electrochemical Society* **2004,** *151*, A1878-A1885.
9. F. Badway, F. C., N. Pereira, and G. G. Amatucci, Carbon Metal Fluoride Nanocomposites High-Capacity Reversible Metal Fluoride Conversion Materials as Rechargeable Positive Electrodes for Li Batteries. *Journal of The Electrochemical Society* · **2003,** *150*, A1318-A1327.
10. Robert E. Doe, K. A. P., Y. Shirley Meng, and Gerbrand Ceder, First-Principles Investigation of the Li-Fe-F Phase Diagram and Equilibrium and Nonequilibrium Conversion Reactions of Iron Fluorides with Lithium. *chemistry of materials* **2008,** *20*, 5274-5283.

11. Naoko Yamakawa, M. J., Baris Key and Clare P. Grey, Identifying the Local Structures Formed during Lithiation of the Conversion Material, Iron Fluoride, in a Li Ion Battery: A Solid-State NMR, X-ray Diffraction, and Pair Distribution Function Analysis Study. *Journal of the American Chemical Society* **2009,** *131*, 10525-10536.
12. Li, L.; Jacobs, R.; Gao, P.; Gan, L.; Wang, F.; Morgan, D.; Jin, S., Origins of Large Voltage Hysteresis in High-Energy-Density Metal Fluoride Lithium-Ion Battery Conversion Electrodes. *Journal of the American Chemical Society* **2016,** *138* (8), 2838-2848.
13. Bai, Y.; Zhou, X.; Jia, Z.; Wu, C.; Yang, L.; Chen, M.; Zhao, H.; Wu, F.; Liu, G., Understanding the combined effects of microcrystal growth and band gap reduction for Fe(1−x)TixF3 nanocomposites as cathode materials for lithium-ion batteries. *Nano Energy* **2015**.
14. Sung-Wook Kim , D.-H. S., Hyeokjo Gwon , Jongsoon Kim , and Kisuk Kang, Fabrication of FeF 3 Nanofl owers on CNT Branches and Their Application to High Power Lithium Rechargeable Batteries. *Advanced materials* **2010,** *22*, 5260-5264.
15. Ting Li, L. L., Yu L. Cao, Xin P. Ai, and Han X. Yang, Reversible Three-Electron Redox Behaviors of FeF3 Nanocrystals as High-Capacity Cathode-Active Materials for Li-Ion Batteries. *Journalof Physical Chemistry C* **2010,** *114*, 3190-3195.
16. Li Liu, M. Z., Lanhua Yi, Haipeng Guo, Jinli Tan, Hongbo Shu, Xiukang Yang, Zhenhua Yang and Xianyou Wang, Excellent cycle performance of Co-doped FeF3/C nanocomposite cathode material for lithium-ion batteries. *Journal of Materials Chemistry* **2002,** *22*, 17539–17550.
17. Wu, W.; Wang, Y.; Wang, X.; Chen, Q.; Wang, X.; Yang, S.; Liu, X.; Guo, J.; Yang, Z., Structure and electrochemical performance of FeF3/V2O5 composite cathode material for lithium-ion battery. *Journal of Alloys and Compounds* **2009,** *486* (1-2), 93-96.
18. Wu, W.; Wang, X.; Wang, X.; Yang, S.; Liu, X.; Chen, Q., Effects of MoS2 doping on the electrochemical performance of FeF3 cathode materials for lithium-ion batteries. *Materials Letters* **2009,** *63* (21), 1788-1790.
19. Bai, Y.; Yang, L.-w.; Wu, F.; Wu, C.; Chen, S.; Bao, L.-y.; Hu, W.-l., High performance FeFx/C composites as cathode materials for lithium-ion batteries. *Journal of Renewable and Sustainable Energy* **2013,** *5* (2), 021402.
20. Chilin Li , X. M., Peter A. van Aken , and Joachim Maier, A High-Capacity Cathode for Lithium Batteries Consisting of Porous Microspheres of Highly Amorphized Iron Fluoride Densifi ed from Its Open Parent Phase. *Advanced Energy Materials* **2013**.
21. Liu, L.; Guo, H.; Zhou, M.; Wei, Q.; Yang, Z.; Shu, H.; Yang, X.; Tan, J.; Yan, Z.; Wang, X., A comparison among FeF3·3H2O, FeF3·0.33H2O and FeF3 cathode materials for lithium ion batteries: Structural, electrochemical, and mechanism studies. *Journal of Power Sources* **2013,** *238*, 501-515.
22. Chilin Li , L. G., Jianwei Tong , Susumu Tsukimoto , and Joachim Maier, A Mesoporous Iron-Based Fluoride Cathode of Tunnel Structure for Rechargeable Lithium Batteries. *Advanced Functional Materials* **2011,** *21*, 1391–1397.
23. Chilin Li, C. Y., Lin Gu, Robert E. Dinnebier, Xiaoke Mu,Peter A. van Aken, and Joachim Maier, An FeF3·0.5H2O Polytype: A Microporous Framework Compound with Intersecting Tunnels for Li and Na Batteries. *Journal of the American Chemical Society* **2013,** *135*, 11425-11428.
24. Chilin Li, L. G., Jianwei Tong, and Joachim Maier,, Carbon Nanotube Wiring of Electrodes for High-Rate Lithium Batteries Using an Imidazolium-Based Ionic Liquid Precursor as Dispersant and Binder: A Case Study on Iron Fluoride Nanoparticles. *ACS Nano* **2011,** *5*, 2930-2938.
25. Chilin Li , L. G., Susumu Tsukimoto , Peter A. van Aken , and Joachim Maier, Low-Temperature Ionic-Liquid-Based Synthesis of Nanostructured Iron-Based Fluoride Cathodes for Lithium Batteries. *Adv. Mater.* **2010,** *22*, 3650–3654.
26. Li, C.; Yin, C.; Mu, X.; Maier, J., Top-Down Synthesis of Open Framework Fluoride for Lithium and Sodium Batteries. *Chemistry of Materials* **2013,** *25* (6), 962-969.
27. Bingjiang Li, D. W. R., Naiqing Zhang, and Kening Sun, An In Situ Ionic-Liquid-Assisted Synthetic Approach to Iron Fluoride/Graphene Hybrid Nanostructures as Superior Cathode Materials for Lithium Ion Batteries. *ACS applied materials & interfaces* **2013,** *5*, 5057-5063.
28. Li, B.; Cheng, Z.; Zhang, N.; Sun, K., Self-supported, binder-free 3D hierarchical iron fluoride flower-like array as high power cathode material for lithium batteries. *Nano Energy* **2014,** *4*, 7-13.
29. Bai, Y.; Zhou, X.; Zhan, C.; Ma, L.; Yuan, Y.; Wu, C.; Chen, M.; Chen, G.; Ni, Q.; Wu, F.; Shahbazian-Yassar, R.; Wu, T.; Lu, J.; Amine, K., 3D Hierarchical nano-flake/micro-flower iron fluoride with hydration water induced tunnels for secondary lithium battery cathodes. *Nano Energy* **2017,** *32*, 10-18.

30. Li, Z.; Wang, B.; Li, C.; Liu, J.; Zhang, W., Hydrogen-bonding-mediated structural stability and electrochemical performance of iron fluoride cathode materials. *J. Mater. Chem. A* **2015,** *3* (31), 16222-16228.
31. Li, B.; Zhang, N.; Sun, K., Confined iron fluoride@CMK-3 nanocomposite as an ultrahigh rate capability cathode for Li-ion batteries. *Small* **2014,** *10* (10), 2039-46.
32. Li, Y.; Zhou, X.; Bai, Y.; Chen, G.; Wang, Z.; Li, H.; Wu, F.; Wu, C., Building an Electronic Bridge via Ag Decoration To Enhance Kinetics of Iron Fluoride Cathode in Lithium-Ion Batteries. *ACS applied materials & interfaces* **2017,** *9* (23), 19852-19860.
33. Tan, J.; Liu, L.; Hu, H.; Yang, Z.; Guo, H.; Wei, Q.; Yi, X.; Yan, Z.; Zhou, Q.; Huang, Z.; Shu, H.; Yang, X.; Wang, X., Iron fluoride with excellent cycle performance synthesized by solvothermal method as cathodes for lithium ion batteries. *Journal of Power Sources* **2014,** *251*, 75-84.
34. Li, Y.; Bai, Y.; Bi, X.; Qian, J.; Ma, L.; Tian, J.; Wu, C.; Wu, F.; Lu, J.; Amine, K., An Effectively Activated Hierarchical Nano-/Microspherical Li1.2Ni0.2Mn0.6O2 Cathode for Long-Life and High-Rate Lithium-Ion Batteries. *ChemSusChem* **2016,** *9* (7), 728-35.
35. Li, Y.; Bai, Y.; Wu, C.; Qian, J.; Chen, G.; Liu, L.; Wang, H.; Zhou, X.; Wu, F., Three-dimensional fusiform hierarchical micro/nano Li1.2Ni0.2Mn0.6O2 with a preferred orientation (110) plane as a high energy cathode material for lithium-ion batteries. *Journal of Materials Chemistry A* **2016,** *4* (16), 5942-5951.
36. Li, Y.; Wu, C.; Bai, Y.; Liu, L.; Wang, H.; Wu, F.; Zhang, N.; Zou, Y., Hierarchical Mesoporous Lithium-Rich Li[Li0.2Ni0.2Mn0.6]O2 Cathode Material Synthesized via Ice Templating for Lithium-Ion Battery. *ACS applied materials & interfaces* **2016,** *8* (29), 18832-40.
37. Wei, G. Z.; Lu, X.; Ke, F. S.; Huang, L.; Li, J. T.; Wang, Z. X.; Zhou, Z. Y.; Sun, S. G., Crystal habit-tuned nanoplate material of Li[Li1/3-2x/3NixMn2/3-x/3]O(2) for high-rate performance lithium-ion batteries. *Advanced materials* **2010,** *22* (39), 4364-7.
38. Shi, Y.-L.; Wu, N.; Shen, M.-F.; Cui, Y.-L.; Jiang, L.; Qiang, Y.-H.; Zhuang, Q.-C., Electrochemical Behavior of Iron(III) Fluoride Trihydrate as a Cathode in Lithium-Ion Batteries. *ChemElectroChem* **2014,** *1* (3), 645-654.
39. Long, Z.; Hu, W.; Liu, L.; Qiu, G.; Qiao, W.; Guan, X.; Qiu, X., Mesoporous Iron Trifluoride Microspheres as Cathode Materials for Li-ion Batteries. *Electrochimica Acta* **2015,** *151*, 355-362.
40. Shi, Y.-L.; Shen, M.-F.; Xu, S.-D.; Zhuang, Q.-C.; Jiang, L.; Qiang, Y.-H., Electrochemical impedance spectroscopy investigation of the FeF3/C cathode for lithium-ion batteries. *Solid State Ionics* **2012,** *222-223*, 23-30.
41. Huggins, W. W. a. R. A., Determination of the Kinetic Parameters of Mixed-Conducting Electrodes and Application to the System Li_8Sb
journal of the electrochemical society **1977,** *124*, 1569-1578.
42. K. M. Shaju, G. V. S. R. a. B. V. R. C., Li ion kinetic studies on spinel cathodes, Li(M1/6Mn11/6)O4 (M ~ Mn, Co, CoAl) by GITT and EIS. *Journal of Materials Chemistry* **2003,** *13*, 106-113.
43. Shaju, K. M.; Subba Rao, G. V.; Chowdari, B. V. R., Electrochemical Kinetic Studies of Li-Ion in O2-Structured Li[sub 2/3](Ni[sub 1/3]Mn[sub 2/3])O[sub 2] and Li[sub (2/3)+x](Ni[sub 1/3]Mn[sub 2/3])O[sub 2] by EIS and GITT. *Journal of The Electrochemical Society* **2003,** *150* (1), A1.
44. Shi, S. J.; Tu, J. P.; Tang, Y. Y.; Yu, Y. X.; Zhang, Y. Q.; Wang, X. L., Synthesis and electrochemical performance of Li1.131Mn0.504Ni0.243Co0.122O2 cathode materials for lithium ion batteries via freeze drying. *Journal of Power Sources* **2013,** *221*, 300-307.
45. Ihm, J. Z., A.; Cohen, M. L.,, Momentum-space Formalism for the Total Energy of Solids. *J. Phys. C: Solid state Phys.* **1979,** *12*, 4409-4421.
46. Perdew, J. P. B., K.; Ernzerhof, M.,, Generalized Gradient Approximation Made Simple. *Phys. Rev. Lett.* **1996,** *77*, 3865-3868.
47. G. Kresse , D. J., From ultrasoft pseudopotentials to the projector augmented-wave method. *Phys. Rev. B* **1999,** *59*, 1758-1775.
48. Kresse, G. F., J., Efficient Iterative Schemes for ab initio Total-energy Calculations Using a Plane-wave Basis Set. *Phys. Rev. B* **1996,** *54*, 11169−11186.
49. Anisimov, V. I.; Solovyev, I. V.; Korotin, M. A.; Czyżyk, M. T.; Sawatzky, G. A., Density-functional theory and NiO photoemission spectra. *Physical Review B* **1993,** *48* (23), 16929-16934.
50. Anisimov, V. I. A., F.; Lichtenstein, A. I., First-principles Calculations of the Electronic Structure and Spectra of Strongly Correlated Systems: the LDA+U Method. *J. Phys.: Condens. Matter.* **1997,** *9*, 767–808.

51. Scanlon, D. O. W., A.; Morgan, B. J.; and Watson, G. W., , An ab initio Study of Reduction of V2O5 through the Formation of Oxygen Vacancies and Li Intercalation. *J. Phys. Chem. C* **2008,** *112*, 9903-9911.
52. Monkhorst, H. J.; Pack, J. D., Special points for Brillouin-zone integrations. *Physical Review B* **1976,** *13* (12), 5188-5192.